nanomaterials

MDPI

Article

Fabrication of Self-Assembled $BiFeO_3/CeO_2$ Nanocatalytic Materials for Efficient Catalytic Dye Degradation

Lin Li, Qi Li, Dongqing Wang, Yubo Zhang, Fei Li, Yaru Zhang * and Tifeng Jiao *

State Key Laboratory of Metastable Materials Science and Technology, Hebei Key Laboratory of Applied Chemistry, Hebei Key Laboratory of Nano-Biotechnology, Hebei Key Laboratory of Heavy Metal Deep-Remediation in Water and Resource Reuse, Yanshan University, Qinhuangdao 066004, China

* Correspondence: yrzhang@ysu.edu.cn (Y.Z.); tfjiao@ysu.edu.cn (T.J.)

Abstract: The catalytic treatment of wastewater serves as an effective way to solve the problem of water pollution, in which non-homogeneous Fenton catalysts are widely used. However, the activity enhancement of non-homogeneous Fenton catalysts still remains a great challenge. Herein, self-assembled $BiFeO_3/CeO_2$ nanocatalytic materials with different molar ratios were successfully fabricated by a suspension blending method, following which the structure evolution was determined by various characterizations. The catalytic degradation of methylene blue (MB), rhodamine B (RhB), and saffron T (ST) were performed over the $BiFeO_3/CeO_2$ nanocatalytic materials. It was found that the $0.2BiFeO_3$:$0.8CeO_2$ nanocatalytic materials exhibited an 80.8% degradation efficiency for RhB. The $0.6BiFeO_3$:$0.4CeO_2$ nanocatalytic materials reached 81.1% and 48.7% for ST and MB, respectively. The $BiFeO_3/CeO_2$ nanocatalytic materials also showed a good stability during several cycles. The combination of CeO_2 with $BiFeO_3$ led to an enhanced activity for dye degradation, probably due to the electron transfer from $\equiv Fe^{2+}$ to $\equiv Ce^{4+}$. This study provides a new approach to dye degradation by using Fenton catalytic systems.

Keywords: CeO_2; $BiFeO_3$; nanocatalytic materials; non-homogeneous Fenton catalysts; dye degradation

Citation: Li, L.; Li, Q.; Wang, D.; Zhang, Y.; Li, F.; Zhang, Y.; Jiao, T. Fabrication of Self-Assembled $BiFeO_3/CeO_2$ Nanocatalytic Materials for Efficient Catalytic Dye Degradation. *Nanomaterials* **2023**, *13*, 2545. https://doi.org/10.3390/nano13182545

Academic Editors: Carlos Lodeiro, Vincenzo Vaiano, Giorgio Vilardi and Alexey Pestryakov

Received: 5 July 2023
Revised: 1 September 2023
Accepted: 11 September 2023
Published: 12 September 2023

1. Introduction

With rapid population growth, water consumption by industry, agriculture, and households continues to increase [1], leading to water pollution as a global issue [2]. Synthetic dyes are among the most harmful chemical pollutants in water [3], and water contaminated by them can cause serious health problems [4,5], hence the need for wastewater treatment. Methods of treating water pollutants can be divided into physical, chemical, and biological methods [6]. However, some organic pollutants are toxic and non-degradable, and cannot be treated by conventional physical or biological methods [7]. Still, advanced oxidation processes (AOPs) in chemical methods can solve this problem [8,9]. Studies have shown that the Fenton process is one of the most cost-effective AOPs [10]. However, the homogeneous Fenton reaction has some disadvantages, such as a narrow optimal pH range and the production of iron-containing sludge [11,12]. Therefore, research focused on heterogeneous Fenton catalysis [13]. The non-homogeneous Fenton reaction solves the problems of pH range extension and stability enhancement; so, it is more commonly used in wastewater treatment [14]. H_2O_2 can be activated by Fe(II) to form a Fenton reaction, and the resulting free radicals (e.g., $\cdot OH^-$) are capable of efficiently degrading dye molecules, further advancing the development of wastewater treatment technologies [15]. Iron oxide, zeolite clay, immobilized iron, and carbon materials are widely used non-homogeneous Fenton catalysts, but many show weak catalytic activity [16]. Therefore, efficient catalysts must be prepared to treat dye wastewater [17].

As an important catalytic material, CeO_2 has attracted the attention of researchers in various catalytic applications for its unique structure and redox properties [18–20]. Lin

et al. prepared PdO/CeO_2 catalysts using the deposition–precipitation method, tested them in the non-homogeneous Fenton degradation of acid orange 7 (AO7), and found that they could remove up to 50% of AO7 [21]. Zhu et al. prepared CuO/CeO_2 catalysts by ultrasonic impregnation and found that the removal rate of diclofenac reached 86.62% by testing [22]. Li et al. prepared $LaFeO_3$/3DOM CeO_2 catalyst and found that it maintained effective catalytic degradation of MB after 10 cycles [23]. In addition, CeO_2 of the same purity is cheaper than other oxides; so, CeO_2 was chosen as the loading in this study [24,25]. $BiFeO_3$ is one of the important perovskite-type oxides that can provide Fe^{3+} irrespective of pH [26]. Therefore, many researchers have combined $BiFeO_3$ with other nanomaterials for dye degradation [27]. Huang et al. successfully prepared CdSe QDs/$BiFeO_3$ composite catalysts using the stirring impregnation method. The degradation of phenol by 0.5CBFO reached 98.5 as compared to 41.5% for BFO in 60 min [28]. Volnistem et al. synthesized a $BiFeO_3/Fe_3O_4$ catalyst for degradation of methylene blue under visible light. The time required for the complete degradation of methylene blue solution was more than seven times faster for samples containing 20% Fe_3O_4 than that needed for $BiFeO_3$ alone [29]. Therefore, CeO_2 and $BiFeO_3$ composite catalysts may achieve good results in dye degradation.

In this study, we fabricated $BiFeO_3/CeO_2$ nanocatalytic materials with different molar ratios for the catalytic degradation of MB, RhB, and ST. The $BiFeO_3/CeO_2$ nanocatalytic materials exhibited an enhanced activity, compared with $BiFeO_3$ or CeO_2 nanoparticles, which might benefit from the electron transfer from $\equiv Fe^{2+}$ to $\equiv Ce^{4+}$. This work offers an effective way for catalytic dye degradation over Fenton catalysts.

2. Experimental Section

2.1. Materials

Cerium(III) nitrate hexahydrate, bismuth(III) nitrate pentahydrate, ferric(III) nitrate nonahydrate, citric acid, MB, and ST were purchased from the Shanghai Aladdin Biochemical Technology Co., Ltd. (Shanghai, China). RhB, hydrogen peroxide, glycol, ammonium hydroxide (25 wt%), and methanol were purchased from the Sinopharm Chemical Reagent Co., Ltd. (Shanghai, China). Nitric acid and hydrochloric acid were purchased from the Tianjin Kermel Chemical Reagent Co., Ltd. (Tianjin, China). All chemicals were used as received without further purification.

2.2. Preparation of $BiFeO_3/CeO_2$ Nanocatalytic Materials

2.2.1. Synthesis of CeO_2 Nanoparticles

CeO_2 nanoparticles were obtained using a homogeneous precipitation method. Typically, 10.91 g of $Ce(NO)_3 \cdot 6H_2O$ was dissolved in 100 mL of aqueous glycol (80 vol%) with vigorous stirring in a 50 °C water bath to obtain a transparent solution. Then, 25 mL of 3.0 M $NH_3 \cdot H_2O$ was added dropwise into the above solution, followed by stirring for 24 h. The resulting precipitate was collected by repeatedly washing with water and centrifugation, followed by drying at 80 °C overnight. The dried precipitate was calcined in air at 500 °C for 1 h, following which the CeO_2 nanoparticles were acquired.

2.2.2. Synthesis of $BiFeO_3$

$BiFeO_3$ was prepared by a sol–gel method. In a typical synthesis, 3 mmol of $Bi(NO)_3 \cdot 5H_2O$ and 3 mmol of $Fe(NO)_3 \cdot 9H_2O$ were dissolved in 50 mL of 0.5 M HNO_3 solution. Afterwards, it was gelatinized by adding 3 mmol of citric acid with vigorous stirring, following which the mixture was dried at 80 °C. The resulting powder was then calcined at 600 °C for 2 h to obtain $BiFeO_3$.

2.2.3. Synthesis of $BiFeO_3/CeO_2$ Nanocatalytic Materials

$BiFeO_3/CeO_2$ nanocatalytic materials with different molar ratios were acquired by a suspension blending method. $BiFeO_3$ and CeO_2 were typically put into separate methanol solutions for ultrasonication to obtain $BiFeO_3$ particles and CeO_2 nanoparticles, respectively. Then, the $BiFeO_3$ and CeO_2 suspensions with a designed molar ratio were mixed with

vigorous stirring. The mixture was then dried at 80 °C through evaporation to obtain the $BiFeO_3/CeO_2$ nanocatalytic materials with a designed molar ratio (0.2:0.8, 0.4:0.6, 0.6:0.4, or 0.8:0.2), which was denoted as $0.2BiFeO_3$:$0.8CeO_2$, $0.4BiFeO_3$:$0.6CeO_2$, $0.6BiFeO_3$:$0.4CeO_2$, or $0.8BiFeO_3$:$0.2CeO_2$.

2.3. Characterization

X-ray diffraction (XRD) data were acquired using a Rigaku Smart Lab diffractometer with Cu Kα radiation. Raman spectra were recorded with a dispersive Horiva Jobin Yvon LabRam HR800 microscope equipped with a He–Ne laser. Nitrogen physisorption was performed with a Micromeritics ASAP 2460 instrument at −196 °C. Scanning electron microscopy (SEM) images and the corresponding element mapping were performed with a field-emission Quanta FEG 250 microscope. Transmission electron microscopy (TEM) images were acquired using a Hitachi HT7700 microscope. X-ray photoelectron spectroscopy (XPS) data were obtained using a Thermofisher ESCALAB 250Xi instrument with monochromated Al Kα radiation as the X-ray source.

2.4. Catalytic Tests for Dye Degradation

The catalytic effect of $BiFeO_3/CeO_2$ nanocatalytic materials was observed by catalyzing the dyes MB, RhB, and ST. Firstly, 20 mg of $BiFeO_3/CeO_2$ nanocatalytic materials with different molar ratios were weighed into 50 mL solutions with concentrations of RhB (12 mg L^{-1}), MB (15 mg L^{-1}), and ST (15 mg L^{-1}), respectively. The mixture solutions were stirred until adsorption and desorption equilibrate in the dark. Subsequently, 30% H_2O_2 was added dropwise to the mixture to reach a concentration of 0.016 M, followed by a dropwise addition of diluted HCL (2.0 M); the pH of the experimental solution was adjusted around 3, and the centrifugal supernatant was isolated at the same intervals. Finally, the absorbance value at the maximum absorption wavelength of the dye was measured, and the removal rate of the dye was calculated and fitted to the kinetic data according to Equations (1)–(3). The catalytic rates of nanocatalytic materials for different dyes were calculated by Equation (1).

$$K = \frac{(A_0 - A_T)}{A_0} \times 100\% \tag{1}$$

where K represents the catalytic rate, A_0 represents the absorbance concentration of the original dye solution, and A_T represents the absorbance at the moment T.

We investigated the adsorption properties of these nanomaterials on the dye solutions by a quasi-first-order kinetic model and a quasi-second-order kinetic model.

Equation (2) is a quasi-first-order kinetic equation:

$$q_t = q_e\left(1 - e^{-k_1 t}\right) \tag{2}$$

Equation (3) is a quasi-second-order kinetic equation:

$$\frac{t}{q_t} = \frac{1}{k_2 q_e^2} + \frac{t}{q_e} \tag{3}$$

where q_e is the adsorption capacity of MB and RhB dyes at equilibrium (mg/g), q_t is the adsorption capacity of MB and RhB dyes at time t (mg/g), and the values of k_1 and k_2 are the quasi-first and quasi-second-order kinetic rate constants, respectively.

When the catalytic process was finished, the cyclic stability experiments of the $BiFeO_3/CeO_2$ nanocatalytic materials were carried out. The composite catalyst with the best catalytic effect was selected, washed with ethanol, and then washed and dried using ultrapure water. The recovered nanocatalytic materials catalysts were then catalyzed for six cycles under the same conditions for the three dyes.

3. Results and Discussion

Next, we performed various structural characterizations of the prepared CeO_2 nanoparticles, $BiFeO_3$ nanoparticles, and $BiFeO_3/CeO_2$ nanocatalytic materials. Figure 1a shows the XRD patterns of CeO_2 nanoparticles, $BiFeO_3$ nanoparticles, and four $BiFeO_3/CeO_2$ nanocatalytic materials with different molar ratios. There are three prominent absorption peaks of CeO_2 with 2θ of 28.54°, 47.48°, and 56.33° corresponding to the crystallographic planes (111), (220), and (311) in the synthesized nanocatalytic materials. The XRD patterns of CeO_2 nanoparticles do not have peaks corresponding to any secondary or impurity phases. The XRD patterns of $BiFeO_3$ particles agree with the JCPDS data (Card No. 71-2494) and reveal a rhombic crystal structure of the $BiFeO_3$ phase with the R3c space group. The well-defined XRD peaks of $BiFeO_3$ particles indicate their enhanced crystallinity. The characteristic diffraction peaks of $BiFeO_3$ and CeO_2 crystalline forms can be represented by the XRD patterns of $BiFeO_3/CeO_2$ nanocatalytic materials. As shown in the figure, the diffraction pattern of the nanocatalytic materials is very similar to that of pure CeO_2 at a $BiFeO_3$ molar ratio of 0.2. When increasing the molar ratio of $BiFeO_3$ in the nanocatalytic material samples, the diffraction patterns are more similar to those of pure $BiFeO_3$, and the peaks at the crystalline plane at (101), (012), (110), and (104) are gradually enhanced. This may be due to the high crystallinity of the $BiFeO_3$ phase and therefore shows as the dominant peak in the XRD spectra of the samples of the nanocatalytic materials.

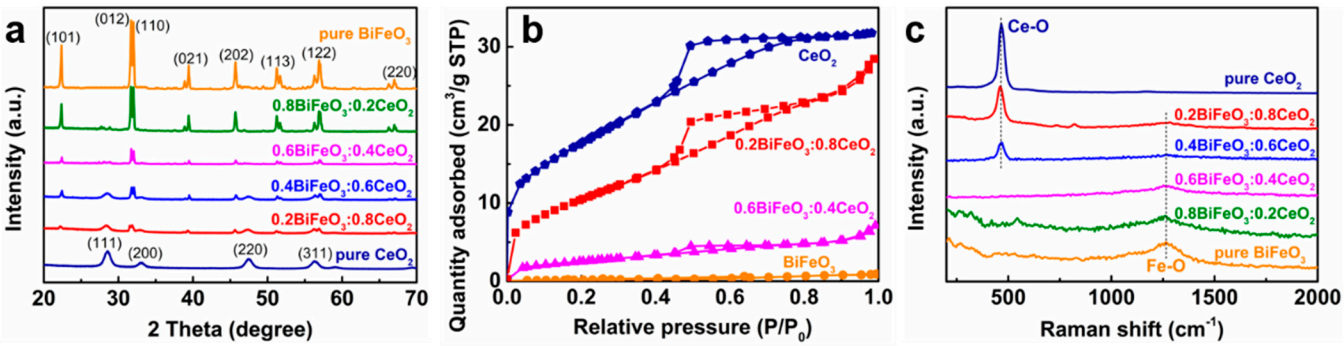

Figure 1. (**a**) XRD patterns of CeO_2, $BiFeO_3$, and $BiFeO_3/CeO_2$ nanocatalytic materials. (**b**) N_2 adsorption–desorption isotherms for CeO_2, $BiFeO_3$, and $BiFeO_3/CeO_2$ nanocatalytic materials. (**c**) Raman spectra of CeO_2, $BiFeO_3$, and $BiFeO_3/CeO_2$ nanocatalytic materials.

Figure 1b shows the N_2 adsorption–desorption isotherms of CeO_2 nanoparticles, $BiFeO_3$ nanoparticles, and $BiFeO_3/CeO_2$ nanocatalytic materials, and the test results are shown in Table 1. As displayed in Figure 1b, the adsorption–desorption of N_2 occurred for CeO_2 nanoparticles and $BiFeO_3/CeO_2$ nanocatalytic materials, but no adsorption–desorption of N_2 occurred for $BiFeO_3$ particles. The adsorption and desorption curves overlap at the relative pressure $P/P_0 < 0.46$, mainly due to the reversible monomolecular layer adsorption. As seen in the figure, $0.2BiFeO_3{:}0.8CeO_2$ adsorbs more N_2 than $0.6BiFeO_3{:}0.4CeO_2$ and the curve of the $BiFeO_3/CeO_2$ nanocatalytic materials has a significant hysteresis at higher relative pressures (P/P_0 = 0.50–0.8), which implies that the nanocatalytic materials have a mesoporous structure. The CeO_2 nanoparticle adsorption belongs to a type IV adsorption, but for the $BiFeO_3$ nanoparticles, N_2 adsorption and desorption were not significant. This may be due to the smooth, flaky nature of $BiFeO_3$ nanoparticles.

Table 1. Physisorption data of CeO_2, $BiFeO_3$, and $BiFeO_3/CeO_2$ nanocatalytic materials.

Sample	BET Surface Area (m^2 g^{-1})	Total Pore Volume (cm^3 g^{-1})	Average Pore Size (nm)
CeO_2	65	0.049	3.03
$0.2BiFeO_3$:$0.8CeO_2$	40	0.044	4.44
$0.6BiFeO_3$:$0.4CeO_2$	9	0.011	4.68
$BiFeO_3$	1	0.001	6.59

Figure 1c shows the Raman spectra of CeO_2, $BiFeO_3$, and four different molar ratios of $BiFeO_3/CeO_2$ nanocatalytic materials. As shown in the figure, the vibration of the Ce–O bond gradually increases, and the vibration of the Fe–O bond gradually decreases with the increase in the $BiFeO_3$ ratio. The successful preparation of the nanocatalytic materials $BiFeO_3/CeO_2$ was further verified.

The SEM images of CeO_2 nanoparticles, $BiFeO_3$ nanoparticles, and $BiFeO_3/CeO_2$ nanocatalytic materials are shown in Figure 2. Figure 2a indicates that the CeO_2 nanoparticles are spherical in shape, small in size, and clustered together. Figure 2b shows the SEM image of the $0.2BiFeO_3$:$0.8CeO_2$ nanocatalytic materials, which has a large particle shape and attached CeO_2 nanoparticles. Figure 2c shows the SEM image of $0.4BiFeO_3$:$0.6CeO_2$ nanocatalytic materials, which shows the structure of pores between each large particle and the attachment of CeO_2 nanoparticles. Figure 2d shows the SEM image of $0.6BiFeO_3$:$0.4CeO_2$ nanocatalytic materials; it can be seen that this nanocatalytic materials appear with many pore structures and different lamellae agglomerated together with a small amount of CeO_2 nanoparticles attached. Figure 2e shows the SEM image of the $0.8BiFeO_3$:$0.2CeO_2$ nanocatalytic materials, where it can be observed that the morphology is a structure of lamellae superimposed on each other and does not have holes. There is a significant difference in the morphology of $BiFeO_3/CeO_2$ nanocatalytic materials with different molar ratios, which may be related to the amount of CeO_2 nanoparticles and the speed and time of stirring. Figure 2f shows the SEM images of the $BiFeO_3$ particles prepared by the sol–gel method, and it is observed that the morphology is irregularly clustered together in sheets and has a pore-like structure. Figure 2g shows the mapping image of the $BiFeO_3/CeO_2$ nanocatalytic materials, and similar elemental distribution results were obtained from different positions in samples. And it can be concluded that the presence of Ce, Fe, and Bi elements proves the successful preparation of the nanocatalytic materials $BiFeO_3/CeO_2$.

The TEM images of CeO_2 nanoparticles, $BiFeO_3$ nanoparticles, and $BiFeO_3/CeO_2$ nanocatalytic materials are shown in Figure 3. Figure 3a shows the TEM image of CeO_2 nanoparticles, which can be observed as CeO_2 nanoparticles are spherical in shape with diameters ranging from 5–10 nm. Figure 3b shows the TEM image of $BiFeO_3$ particles, which can be observed to be irregularly flaky and with a diameter of about 0.2 μm. Figure 3c–f show the TEM images of $BiFeO_3/CeO_2$ nanocatalytic materials with different scales, from which it can be observed that many CeO_2 nanoparticles are attached to $BiFeO_3$ particles, which, combined with the SEM images, further indicates that $BiFeO_3/CeO_2$ nanocatalytic materials are successfully prepared.

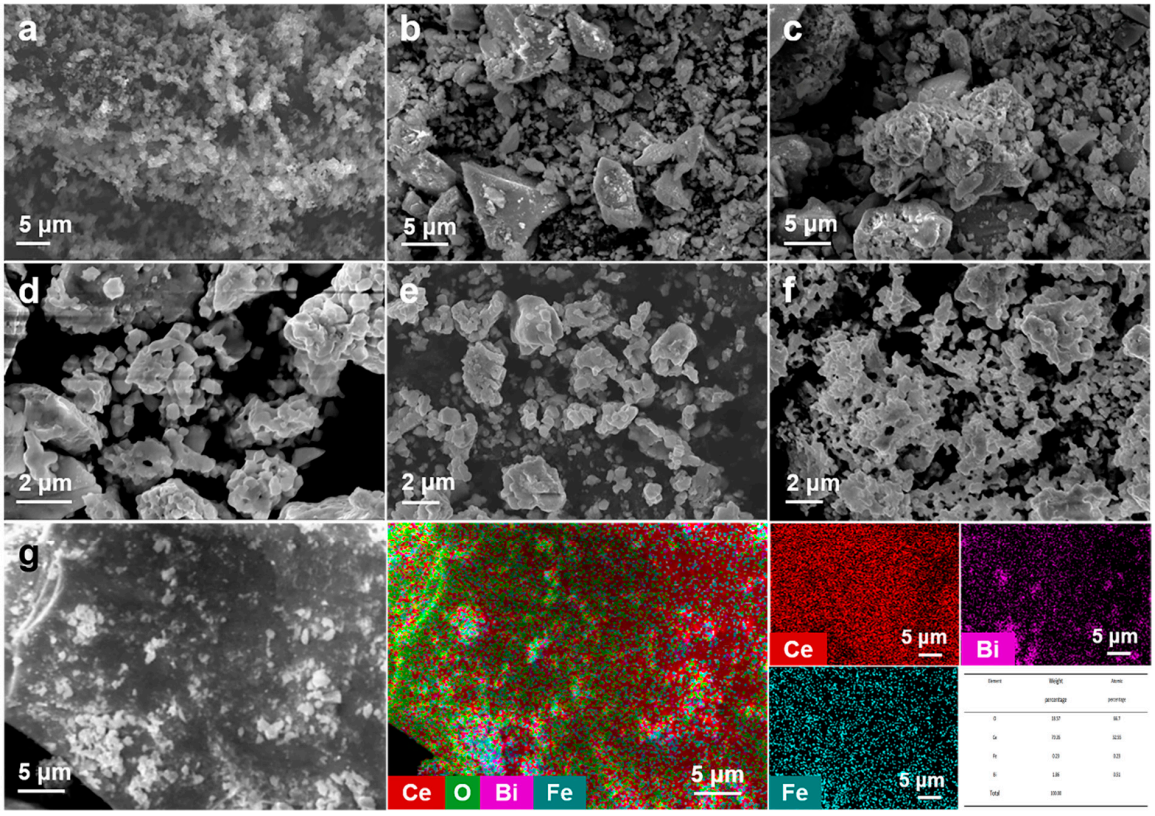

Figure 2. SEM images of (**a**) CeO_2, (**b**) $0.2BiFeO_3$:$0.8CeO_2$, (**c**) $0.4BiFeO_3$:$0.6CeO_2$, (**d**) $0.6BiFeO_3$:$0.4CeO_2$, (**e**) $0.8BiFeO_3$:$0.2CeO_2$, and (**f**) $BiFeO_3$. (**g**) SEM image of the $0.4BiFeO_3$:$0.6CeO_2$ and the corresponding elemental content and mapping of Ce/Bi/Fe in catalytic material.

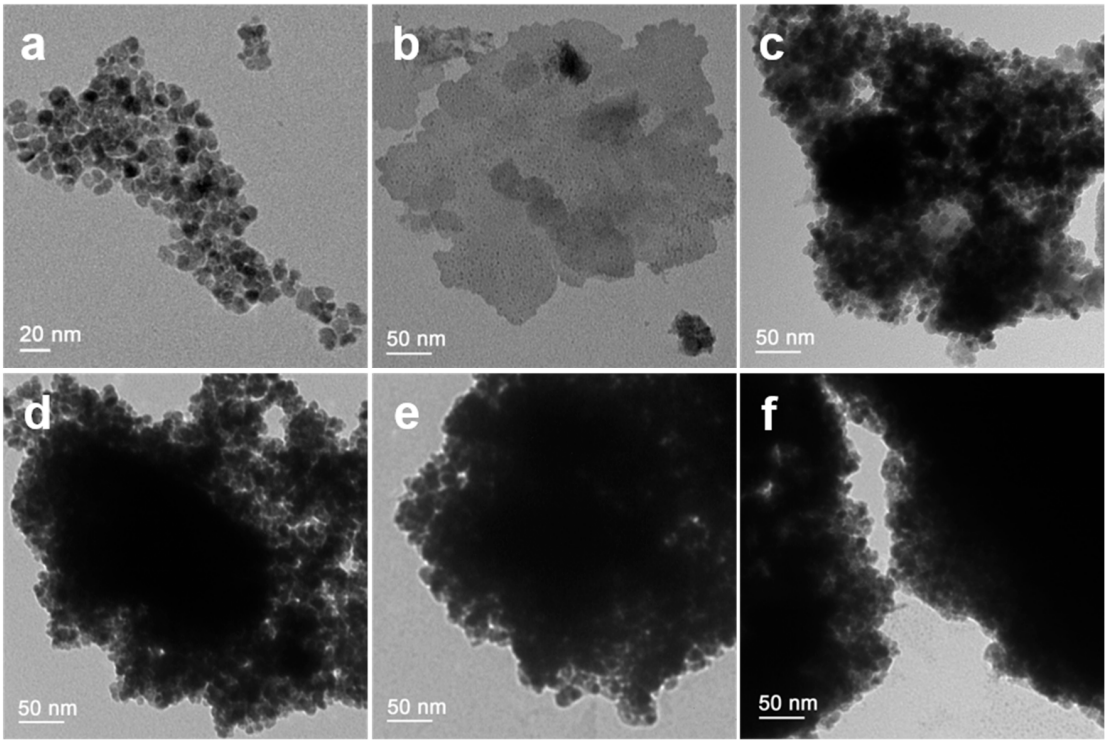

Figure 3. TEM images of (**a**) CeO_2, (**b**) $BiFeO_3$, (**c**) $0.2BiFeO_3$:$0.8CeO_2$, (**d**) $0.4BiFeO_3$:$0.6CeO_2$, (**e**) $0.6BiFeO_3$:$0.4CeO_2$, and (**f**) $0.8BiFeO_3$:$0.2CeO_2$.

Figure 4 shows the XPS spectrum of the $0.6BiFeO_3$:$0.4CeO_2$ nanocatalytic materials. As shown in Figure 4a, the Ce 3d spectrum is decomposed into eight groups. The Ce 4f orbitals interact with the O 2p hybridization, and the four peaks labeled v (882.4 eV), v′ (885.3 eV), v″ (889.0 eV), and v‴ (898.4 eV) belong to Ce $3d_{5/2}$, and the peaks labeled u (900.7 eV), u′ (903.6 eV), u″ (907.3 eV), and u‴ (916.7 eV) are assigned to Ce $3d_{3/2}$. Of the eight peaks, v′ and u′ originate from the Ce^{3+} ion (Ce_2O_3), while the remaining six peaks correspond to the Ce^{4+} species (CeO_2) [30]. The concentration of Ce^{3+} can be related to the surface oxygen vacancies; so, the formation of oxygen vacancies is always accompanied by the formation of Ce^{3+}. In the $BiFeO_3$ phase, the stable oxidation state of Fe is +3, which may also have Fe^{2+}. This can also be confirmed by the Fe spectrum of its $BiFeO_3$ nanostructure. The oxygen core spectrum in Figure 4b shows peaks corresponding to lattice oxygen (O_L) and chemisorbed oxygen/other species (O_{ads}) adsorbed on the surface of the $BiFeO_3/CeO_2$ nanostructure. Peaks of element O appear at 529.5 eV and 532.4 eV, indicating lattice (O_L) and chemisorbed oxygen species (Oads), respectively. The XPS spectrum of Bi 4f of the sample is shown in Figure 4c. The characteristic spectrum of Bi4f consists of two characteristic peaks corresponding to the spin double Bi $4f_{7/2}$ and Bi $4f_{5/2}$, which correspond to binding energy magnitudes of 158.8 eV and 164.1 eV, indicating that the Bi element in the $BiFeO_3/CeO_2$ nanocatalytic materials is of +3 valence. As shown in Figure 4d, the peak of the Fe $2p_{3/2}$ line corresponding to Fe^{2+} appears at 710.0 eV, and the Fe $2p_{3/2}$ line corresponds to Fe^{3+} at 711.0 eV [31]. Figure 4d calculates Fe^{3+}:Fe^{2+} = 55%:45%, which indicates that BFO has slightly more Fe^{3+} ions than Fe^{2+} particles. It indicates that the compounded $BiFeO_3$ particles have multiple oxidation states (Fe^{2+}/Fe^{3+}), and Fe ions usually lead to oxygen vacancies in the $BiFeO_3$.

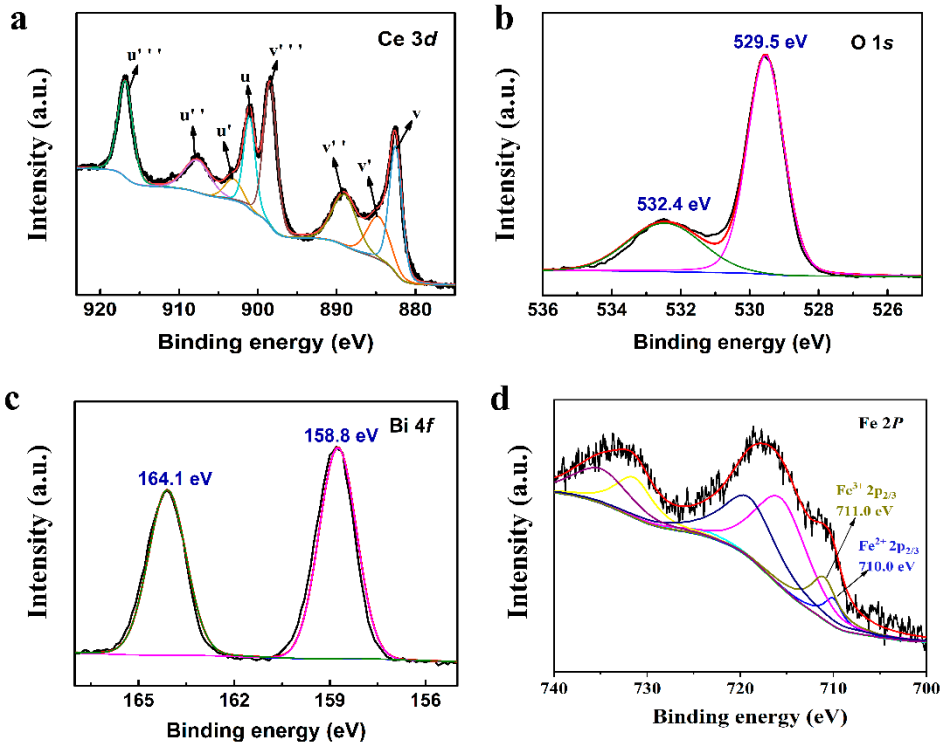

Figure 4. XPS of the $0.6BiFeO_3$:$0.4CeO_2$ nanocatalytic materials. (**a**) Ce 3*d*. (**b**) O 1*s*. (**c**) Bi 4*f*. (**d**) Fe 2*p*.

The catalytic properties of CeO_2 nanoparticles, $BiFeO_3$ nanoparticles, and $BiFeO_3/CeO_2$ nanocatalytic materials on different dyes were investigated as follows. Figure 5 shows the adsorption kinetic results curves of CeO_2, $BiFeO_3$, and $BiFeO_3/CeO_2$ nanocatalytic materials for the degradation of RhB (a,d,g), MB (b,e,h) and ST (c,f,i). Table 2 shows its fitting according to the quasi-first-order kinetic Equation (2) and quasi-second-order kinetic Equation (3) to make the kinetic curves of each of the three dyes.

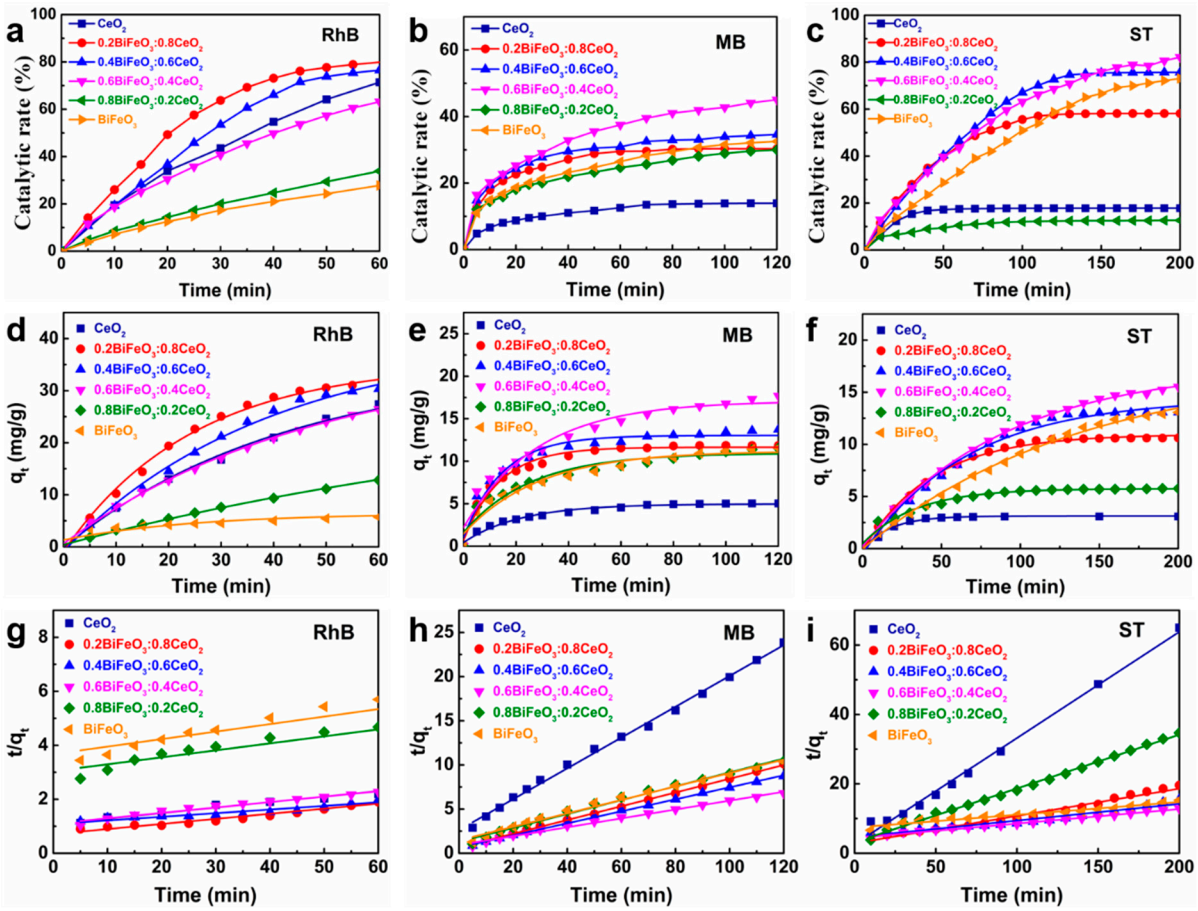

Figure 5. Adsorption kinetic results for degradation of (**a**,**d**,**g**) RhB, (**b**,**e**,**h**) MB, and (**c**,**f**,**i**) ST over CeO_2, $BiFeO_3$, and $BiFeO_3/CeO_2$ nanocatalytic materials.

Table 2. Adsorption fitting data for degradation of RhB, MB, and ST over CeO_2, $BiFeO_3$, and $BiFeO_3/CeO_2$ nanocatalytic materials.

Dye	Catalyst	Pseudo-First-Order Kinetics			Pseudo-Second-Order Kinetics		
		q_e (mg g^{-1})	R^2	K_1 (10^{-2} min^{-1})	q_e (mg g^{-1})	R^2	K_2 (10^{-4} g mg^{-1} min^{-1})
RhB	CeO_2	27.31	0.996	2.380	49.02	0.984	3.857
	$0.2BiFeO_3$:$0.8CeO_2$	32.13	0.995	4.048	52.94	0.958	5.050
	$0.4BiFeO_3$:$0.6CeO_2$	31.04	0.994	2.539	74.29	0.915	1.677
	$0.6BiFeO_3$:$0.4CeO_2$	26.29	0.999	2.087	49.95	0.988	3.661
	$0.8BiFeO_3$:$0.2CeO_2$	13.03	0.999	0.884	38.61	0.950	2.209
	$BiFeO_3$	5.83	0.874	3.967	35.98	0.966	2.102
MB	CeO_2	4.97	0.973	4.562	5.73	0.997	115.498
	$0.2BiFeO_3$:$0.8CeO_2$	11.65	0.978	7.274	12.85	0.999	92.706
	$0.4BiFeO_3$:$0.6CeO_2$	13.03	0.966	6.867	14.73	0.999	68.080
	$0.6BiFeO_3$:$0.4CeO_2$	17.09	0.958	3.557	19.93	0.992	26.842
	$0.8BiFeO_3$:$0.2CeO_2$	10.95	0.934	3.937	12.77	0.990	46.602
	$BiFeO_3$	11.20	0.953	3.504	13.13	0.990	39.497
ST	CeO_2	3.12	0.990	5.717	3.27	0.993	357.392
	$0.2BiFeO_3$:$0.8CeO_2$	10.96	0.997	2.288	12.71	0.976	21.482
	$0.4BiFeO_3$:$0.6CeO_2$	14.38	0.990	1.515	20.81	0.947	5.012
	$0.6BiFeO_3$:$0.4CeO_2$	17.44	0.998	1.114	23.98	0.988	3.969
	$0.8BiFeO_3$:$0.2CeO_2$	5.75	0.975	3.010	6.44	0.997	76.517
	$BiFeO_3$	13.35	0.997	0.726	27.19	0.959	1.829

Figure 5a–c show that the catalytic rate of CeO_2 nanoparticles, $BiFeO_3$ particles, and $BiFeO_3/CeO_2$ nanocatalytic materials in catalyzing the dye solution started fast and then gradually slowed down to a stationary value. The fast catalytic rate at the beginning is because the concentration difference between the dye and the catalyst is relatively apparent, and the amount of H_2O_2 is sufficient to produce a large amount of ·OH by fully interacting with the catalyst under acidic conditions. As the catalytic reaction proceeds, the amount of H_2O_2 and the dye concentration gradually decrease; so, the catalytic rate slows. It can also be observed that there is a significant difference in the catalytic effect of CeO_2, $BiFeO_3$, and different molar ratios of $BiFeO_3/CeO_2$ for other dyes. The catalytic efficiency of each molar ratio catalyst can only reach a maximum of 47.9% for MB dye solution within 120 min, while it can reach more than 80.0% for RhB and ST dye solutions. Among them, the nanocatalytic materials with a molar ratio of $0.2BiFeO_3$:$0.8CeO_2$ could achieve the maximum catalytic efficiency of 80.8% for RhB within 60 min, while the nanocatalytic materials with a molar ratio of $0.6BiFeO_3$:$0.4CeO_2$ could reach 81.1% and 48.7% for ST and MB dye degradation, respectively. As also shown in Figure 5, the correlation coefficients R^2 of the fitted quasi-first-order and quasi-second-order models differed very little and were close to 1. Therefore, the quasi-first-order and quasi-second-order models could simulate the process of dye solutions catalyzed by CeO_2, $BiFeO_3$, and $BiFeO_3/CeO_2$ nanocatalytic materials with different molar ratios more accurately. For RhB dye solutions, the catalytic amount of nanocatalytic materials with a molar ratio of $0.2BiFeO_3$:$0.8CeO_2$ reaches 32.1 mg/g, larger than the other ratios. For MB and ST dye solutions, the nanocatalytic materials with a molar ratio of $0.6BiFeO_3$:$0.4CeO_2$ had the highest catalytic amount per unit, reaching 17.1 mg/g and 17.4 mg/g, respectively. The effect of the catalysts with different molar ratios was different for other dyes, possibly due to the pH at the time of catalysis or the amount of H_2O_2 added.

The $0.6BiFeO_3$:$0.4CeO_2$ catalysts at the end of the experiment were collected by centrifugation and then washed clean with anhydrous ethanol and ultrapure water before drying and collecting in an oven. The dried catalysts were repeated six times for the dye-catalyzed solution experiments under the same conditions, and the obtained experimental results are shown in Figure 6. The data show that after repeated cycling experiments conducted several times, the catalytic efficiencies of this sample for RhB, MB, and ST dye solutions were 83.5%, 88.7%, and 90.4% of the first time, respectively, indicating that the $0.6BiFeO_3$:$0.4CeO_2$ nanocatalytic materials have good cyclable stability.

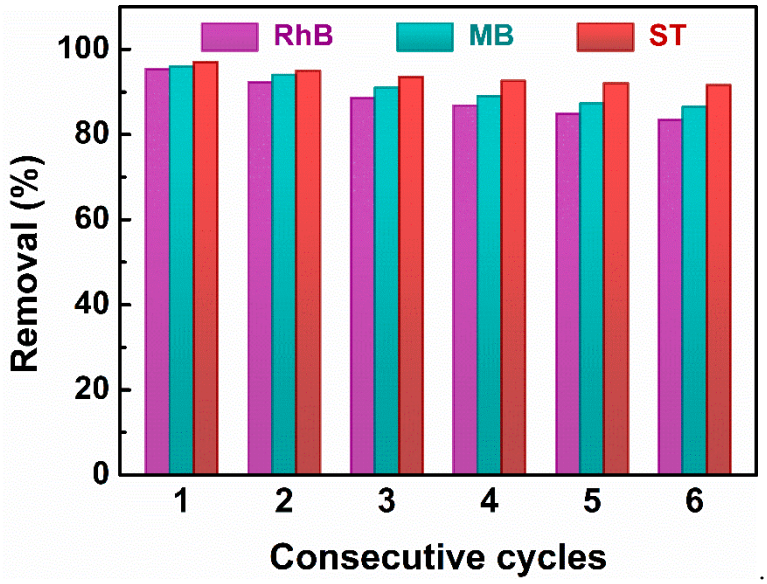

Figure 6. Cycling stability of the $0.6BiFeO_3$:$0.4CeO_2$ nanocatalytic materials for degradation of RhB, MB, and ST.

Figure 7 shows the reaction mechanism of $BiFeO_3/CeO_2$ nanocatalytic materials for the activation of H_2O_2 under acidic conditions. First, the reaction of Fe^{3+} species with H_2O_2 (Equation (4)) and $HO_2\cdot$(Equation (5)) generates many $\equiv Fe^{2+}$ species. The standard redox potential of Ce^{4+}/Ce^{3+} is 1.44 V, and Fe^{3+}/Fe^{2+} is 0.77 V (Equations (6)–(8)). Therefore, the transfer of electrons from $\equiv Fe^{2+}$ to $\equiv Ce^{4+}$ (Equation (6)) is thermodynamically favorable [16]. Based on previous work, we know that cerium can cycle redox in the presence of H_2O_2 and produce $\cdot OH_{ads}$ (Equations (7)–(9)), which behaves similarly to iron in Fenton-like reactions [32]. The iron ions above $BiFeO_3$ are dispersed in the native solution and trigger the decomposition of H_2O_2 by chain reactions (Equations (10)–(12)) to produce $\cdot OH$ free radical. A small number of $\cdot OH_{ads}$ can diffuse from the catalyst surface into the native solution. As shown in Equations (13)–(18), competing reactions may negatively affect oxidation. Finally, the hydroxyl radicals, which are self-carried on the catalyst surface and in the solution, decompose the dye solution.

$$\equiv Fe^{3+} + H_2O_2 \rightarrow \equiv Fe^{2+} + OH_2\cdot + H^+ \quad (4)$$

$$\equiv Fe^{3+} + OH_2\cdot \rightarrow \equiv Fe^{2+} + O_2 + H^+ \quad (5)$$

$$\equiv Ce^{4+} + \equiv Fe^{2+} \rightarrow \equiv Ce^{3+} + \equiv Fe^{3+} \quad (6)$$

$$\equiv Ce^{3+} + H_2O_2 + H^+ \rightarrow \equiv Ce^{4+} + \cdot OH_{ads} + H_2O \quad (7)$$

$$\cdot OH_{ads} + H_2O_2 \rightarrow HO_2{}^- + H_2O \quad (8)$$

$$\equiv Ce^{4+} + HO_2{}^- \rightarrow \equiv Ce^{3+} + H^+ + O_2 \quad (9)$$

$$Fe^{2+} + H_2O_2 + H^+ \rightarrow Fe^{3+} + \cdot OH_{free} + H_2O \quad (10)$$

$$Fe^{3+} + H_2O_2 \rightarrow Fe^{2+} + HO_2\cdot + H^+ \quad (11)$$

$$Fe^{3+} + HO_2\cdot \rightarrow Fe^{2+} + O_2 + H^+ \quad (12)$$

$$\cdot OH + Fe^{2+} \rightarrow OH^- + Fe^{3+} \quad (13)$$

$$\cdot OH + H_2O_2 \rightarrow H_2O + HO_2\cdot \quad (14)$$

$$Fe^{2+} + HO_2\cdot \rightarrow Fe^{3+} + HOO^+ \quad (15)$$

$$HO_2\cdot + HO_2\cdot \rightarrow H_2O_2{}^+ + O \quad (16)$$

$$\cdot OH + HO_2\cdot(O_2\cdot{}^-) \rightarrow O_2 + H_2O\ (+OH^-) \quad (17)$$

$$\cdot OH + \cdot OH \rightarrow H_2O_2 \quad (18)$$

$$\cdot OH + \text{dye} \rightarrow \text{degraded products} \quad (19)$$

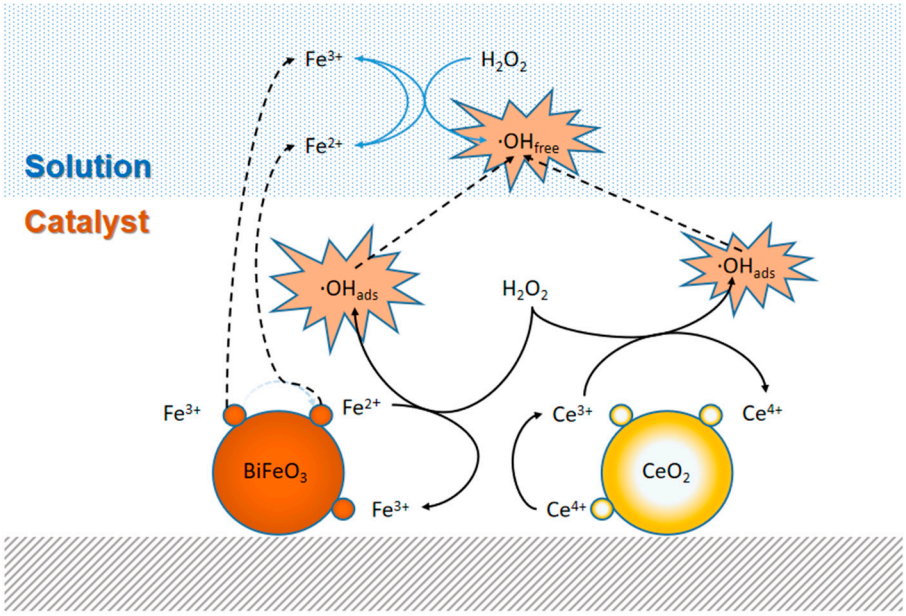

Figure 7. A proposed mechanism for catalytic dye degradation over the $BiFeO_3/CeO_2$ nanocatalytic materials.

4. Conclusions

In conclusion, $BiFeO_3/CeO_2$ nanocatalytic materials with different molar ratios were synthesized and characterized using various techniques. The combination of CeO_2 nanoparticles with $BiFeO_3$ greatly increased the catalytic activity for the degradation of MB, RhB, and ST. The $BiFeO_3/CeO_2$ nanocatalytic materials also showed good stability during six consecutive cycles. The electron transfer from $\equiv Fe^{2+}$ to $\equiv Ce^{4+}$ within the $BiFeO_3/CeO_2$ nanocatalytic materials might dominate the catalytic activity of dye degradation. This finding provides an effective way for activity enhancement of catalytic degradation over Fenton catalytic systems.

Author Contributions: L.L. performed the experiments and wrote the paper. Q.L. performed the experiments. D.W. curated data. Y.Z. (Yubo Zhang) curated data. F.L. curated data. Y.Z. (Yaru Zhang) designed the experiments, and reviewed and edited. T.J. designed the experiments, and reviewed and edited. All authors have read and agreed to the published version of the manuscript.

Funding: This study was supported by the National Natural Science Foundation of China (Nos. 22072127, 22208281, 22372143), the Natural Science Foundation of Hebei Province (No. B2021203016), the Science and Technology Project of Hebei Education Department (No. ZD2022147), and the Special Project for Local Science and Technology Development Guided by the Central Government of China (Nos. 216Z1301G, 226Z1401G, 236Z1201G, 236Z1401G, 236Z1206G).

Institutional Review Board Statement: Not applicable.

Informed Consent Statement: Not applicable.

Data Availability Statement: Not applicable.

Conflicts of Interest: The authors declare no conflict of interest.

References

1. Bilinska, L.; Gmurek, M. Novel trends in AOPs for textile wastewater treatment. Enhanced dye by-products removal by catalytic and synergistic actions. *Water Resour. Ind.* **2021**, *26*, 100160. [CrossRef]
2. Lu, F.; Astruc, D. Nanocatalysts and other nanomaterials for water remediation from organic pollutants. *Coord. Chem. Rev.* **2020**, *408*, 213180. [CrossRef]

3. Mota, H.P.; Quadrado, R.F.N.; Burgo, T.A.L.; Iglesias, B.A.; Fajardo, A.R. Polysaccharide/Fe(III)-porphyrin hybrid film as catalyst for oxidative decolorization of toxic azo dyes: An approach for wastewater treatment. *Arab. J. Chem.* **2020**, *13*, 5923–5938. [CrossRef]
4. Singh, A.; Pal, D.B.; Mohammad, A.; Alhazmi, A.; Haque, S.; Yoon, T.; Srivastava, N.; Gupta, V.K. Biological remediation technologies for dyes and heavy metals in wastewater treatment: New insight. *Bioresour. Technol.* **2022**, *343*, 126154. [CrossRef]
5. An, S.; Zhang, G.; Wang, T.; Zhang, W.; Li, K.; Song, C.; Miller, J.T.; Miao, S.; Wang, J.; Guo, X. High-Density Ultra-small Clusters and Single-Atom Fe Sites Embedded in Graphitic Carbon Nitride (g-C3N4) for Highly Efficient Catalytic Advanced Oxidation Processes. *ACS Nano* **2018**, *12*, 9441–9450. [CrossRef]
6. Luo, H.W.; Zeng, Y.F.; He, D.Q.; Pan, X.L. Application of iron-based materials in heterogeneous advanced oxidation processes for wastewater treatment: A review. *Chem. Eng. J.* **2021**, *407*, 127191. [CrossRef]
7. Xiang, Y.; Liu, H.; Zhu, E.; Yang, K.; Yuan, D.; Jiao, T.; Zhang, Q.; Tang, S. Application of inorganic materials as heterogeneous cocatalyst in Fenton/Fenton-like processes for wastewater treatment. *Sep. Purif. Technol.* **2022**, *295*, 121293. [CrossRef]
8. Yan, Q.Y.; Zhang, J.L.; Xing, M.Y. Cocatalytic Fenton Reaction for Pollutant Control. *Cell Rep. Phys. Sci.* **2020**, *1*, 100149. [CrossRef]
9. Saravanakumar, K.; Park, C.M. Rational design of a novel LaFeO3/g-C3N4/BiFeO3 double Z-scheme structure: Photocatalytic performance for antibiotic degradation and mechanistic insight. *Chem. Eng. J.* **2021**, *423*, 130076. [CrossRef]
10. Zhu, Y.; Zhu, R.; Xi, Y.; Zhu, J.; Zhu, G.; He, H. Strategies for enhancing the heterogeneous Fenton catalytic reactivity: A review. *Appl. Catal. B* **2019**, *255*, 117739. [CrossRef]
11. Yu, Q.; Dai, Y.; Zhang, Z.; Feng, B. Photo-Fenton enhanced degradation of antibiotic by Fe single-atom material: Mechanism, performance and adaptability. *Sep. Purif. Technol.* **2023**, *310*, 123149. [CrossRef]
12. Toor, U.A.; Duong, T.T.; Ko, S.Y.; Hussain, F.; Oh, S.E. Optimization of Fenton process for removing TOC and color from swine wastewater using response surface method (RSM). *J. Environ. Manag.* **2021**, *279*, 111625. [CrossRef] [PubMed]
13. Nie, X.; Li, G.; Li, S.; Luo, Y.; Luo, W.; Wan, Q.; An, T. Highly efficient adsorption and catalytic degradation of ciprofloxacin by a novel heterogeneous Fenton catalyst of hexapod-like pyrite nanosheets mineral clusters. *Appl. Catal. B* **2022**, *300*, 120734. [CrossRef]
14. Dong, H.; Zou, Y.; Zhang, K.; Sun, Y.; Hui, B.; Yang, D.; Cai, L.; Li, J. Biomimetic design of wood carbon-based heterogeneous catalysts for enhanced organic pollutants degradation. *Chem. Eng. J.* **2023**, *451*, 138568. [CrossRef]
15. Wang, F.; Dong, W.; Zhao, Z.; Wang, H.; Li, W.; Zhang, L.; Ouyang, H.; Huang, X.; Li, J. Mechanistic insights into Fe(II)-citric acid complex catalyzed CaO(2) Fenton-like process for enhanced benzo[a]pyrene removal from black-odor sediment at circumneutral pH. *Water Res.* **2022**, *226*, 119233. [CrossRef]
16. Xu, L.; Wang, J. Magnetic nanoscaled Fe_3O_4/CeO_2 composite as an efficient Fenton-like heterogeneous catalyst for degradation of 4-chlorophenol. *Environ. Sci. Technol.* **2012**, *46*, 10145–10153. [CrossRef]
17. He, K.; Chen, G.; Zeng, G.; Chen, A.; Huang, Z.; Shi, J.; Huang, T.; Peng, M.; Hu, L. Three-dimensional graphene supported catalysts for organic dyes degradation. *Appl. Catal. B* **2018**, *228*, 19–28. [CrossRef]
18. Divya, T.; Renuka, N.K. Modulated heterogeneous Fenton-like activity of 'M' doped nanoceria systems (M = Cu, Fe, Zr, Dy, La): Influence of reduction potential of doped cations. *J. Mol. Catal. A Chem.* **2015**, *408*, 41–47. [CrossRef]
19. Chong, S.; Zhang, G.; Zhang, N.; Liu, Y.; Zhu, J.; Huang, T.; Fang, S. Preparation of FeCeOx by ultrasonic impregnation method for heterogeneous Fenton degradation of diclofenac. *Ultrason. Sonochem* **2016**, *32*, 231–240. [CrossRef]
20. Saravanakumar, K.; Ramjan, M.M.; Suresh, P.; Muthuraj, V. Fabrication of highly efficient visible light driven Ag/CeO_2 photocatalyst for degradation of organic pollutants. *J. Alloys Compd.* **2016**, *664*, 149–160. [CrossRef]
21. Ge, L.; Zang, C.; Chen, F. The enhanced Fenton-like catalytic performance of PdO/CeO_2 for the degradation of acid orange 7 and salicylic acid. *Chin. J. Catal.* **2015**, *36*, 314–321. [CrossRef]
22. Zhu, J.; Zhang, G.; Xian, G.; Zhang, N.; Li, J. A High-Efficiency CuO/CeO(2) Catalyst for Diclofenac Degradation in Fenton-Like System. *Front. Chem.* **2019**, *7*, 796. [CrossRef] [PubMed]
23. Li, C.; Li, Z.; Xiaofei, C.; Qinqin, Z.; Haojie, Q.; Xin, Y.; Qian, X.; Zhanwei, T.; Chenyang, Z.; Weitao, M. Novel 3DOM CeO_2 Supported $LaFeO_3$ as an Effective Heterogeneous Fenton Catalyst for Degradation of Methylene Blue. *J. Environ. Eng.* **2022**, *148*, 04022057. [CrossRef]
24. Xiao, R.; Zhang, Y.; Wang, S.; Zhu, H.; Song, H.; Chen, G.; Lin, H.; Zhang, J.; Xiong, J. Prussian blue modified CeO(2) as a heterogeneous photo-Fenton-like catalyst for degradation of norfloxacin in water. *Environ. Sci. Pollut. Res. Int.* **2021**, *28*, 69301–69313. [CrossRef]
25. Sutton, J.E.; Danielson, T.; Beste, A.; Savara, A. Below-Room-Temperature C-H Bond Breaking on an Inexpensive Metal Oxide: Methanol to Formaldehyde on CeO2(111). *J. Phys. Chem. Lett.* **2017**, *8*, 5810–5814. [CrossRef]
26. Di, L.; Yang, H.; Xian, T.; Liu, X.; Chen, X. Photocatalytic and Photo-Fenton Catalytic Degradation Activities of Z-Scheme Ag(2)S/BiFeO(3) Heterojunction Composites under Visible-Light Irradiation. *Nanomaterials* **2019**, *9*, 399. [CrossRef]
27. Guo, Y.S.; Pu, Y.P.; Cui, Y.F.; Hui, C.Y.; Wan, J.; Cui, C.W. A simple method using citric acid as the template agent to improve photocatalytic performance of $BiFeO_3$ nanoparticles. *Mater. Lett.* **2017**, *196*, 57–60. [CrossRef]
28. Huang, T.; Zhu, J.D.; Ge, S.Z.; Guo, T.Y.; Jiang, C.W.; Xie, L. Synthesis of novel CdSe QDs/$BiFeO_3$ composite catalysts and its application for the photo-Fenton catalytic degradation of phenol. *J. Environ. Chem. Eng.* **2020**, *8*, 104384. [CrossRef]
29. Volnistem, E.A.; Bini, R.D.; Silva, D.M.; Rosso, J.M.; Dias, G.S.; Cótica, L.F.; Santos, I.A. Intensifying the photocatalytic degradation of methylene blue by the formation of $BiFeO_3/Fe_3O_4$ nanointerfaces. *Ceram. Int.* **2020**, *46*, 18768–18777. [CrossRef]

30. Jiang, F.; Wang, S.S.; Liu, B.; Liu, J.; Wang, L.; Xiao, Y.; Xu, Y.B.; Liu, X.H. Insights into the Influence of CeO_2 Crystal Facet on CO_2 Hydrogenation to Methanol over Pd/CeO_2 Catalysts. *ACS Catal.* **2020**, *10*, 11493–11509. [CrossRef]
31. Yamashita, T.; Hayes, P. Analysis of XPS spectra of Fe^{2+} and Fe^{3+} ions in oxide materials. *Appl. Surf. Sci.* **2008**, *254*, 2441–2449. [CrossRef]
32. Heckert, E.G.; Seal, S.; Self, W.T. Fenton-like reaction catalyzed by the rare earth inner transition metal cerium. *Environ. Sci. Technol.* **2008**, *42*, 5014–5019. [CrossRef] [PubMed]